Numerical study of the effect of water content on OH production in a pulsed-dc atmospheric pressure helium–air plasma jet*

Mu-Yang Qian(钱沐杨)[1,†], Cong-Ying Yang(杨从影)[2], Zhen-dong Wang(王震东)[1,‡], Xiao-Chang Chen(陈小昌)[1], San-Qiu Liu(刘三秋)[1], and De-Zhen Wang(王德真)[3]

[1] *Department of Physics, Nanchang University, Nanchang* 330031, *China*
[2] *School of Medical, Nanchang University, Nanchang* 330031, *China*
[3] *School of Physics and Optoelectronic Technology, Dalian University of Technology, Dalian* 116023, *China*

(Received 1 September 2015; revised manuscript received 27 October 2015; published online 30 November 2015)

A numerical study of the effect of water content on OH production in a pulsed-dc atmospheric pressure helium–air plasma jet is presented. The generation and loss mechanisms of the OH radicals in a positive half-cycle of the applied voltage are studied and discussed. It is found that the peak OH density increases with water content in air (varying from 0% to 1%) and reaches 6.3×10^{18} m^{-3} when the water content is 1%. Besides, as the water content increases from 0.01% to 1%, the space-averaged reaction rate of three-body recombination increases dramatically and is comparable to those of main OH generation reactions.

Keywords: atmospheric pressure plasma jet, OH radicals, plasma simulation

PACS: 52.50.Dg, 52.65.Kj, 52.80.–s **DOI:** 10.1088/1674-1056/25/1/015202

1. Introduction

In the last two decades, atmospheric pressure plasma jets (APPJs) have received a lot of attention and shown considerable promise in a wide range of practical applications, including biomedical, environmental, and materials processing applications.[1–4] These plasmas can be driven by nanosecond dc voltage pulses with kilohertz repetition frequencies as well as with sine-wave excitations in the kilohertz-to-megahertz range. One important advantage of the nanosecond pulsed discharges over sine-wave excitation is the ability to generate a large number of high energy electrons during the breakdown process.[5,6] Studies have found that OH radicals generated by pulsed-dc APPJs play a very important role in the above listed applications.

The influence of water admixture on the plasma discharges has already been studied by laser-induced fluorescence (LIF) measurement and computational modeling in the past.[7–13] Li *et al.*[7] investigated the effect of water vapor addition (varying from 0% to 1%) on OH generation in the Ar–H_2O admixture atmospheric RF plasma jet by spatially resolved LIF. Liu *et al.*[8] studied the production mechanism of OH radicals in a pulsed-dc APPJs by two-dimensional and one-dimensional discharge model. Ono *et al.*[9,10] studied the dynamics of OH radicals in pulsed corona plasma discharge in a humid-air environment. Pei *et al.*[11,12] proposed an OH density model, which included the main generation processes of OH and gas flow effect. Verreycken *et al.*[13] studied the production of OH in a pin–pin nanosecond pulsed filamentary discharge and also gave the absolute OH density. However, most of these results have aimed at time-averaged OH density. On the other hand, the OH generation process in a single pulse cycle, especially during the rising breakdown process, is very important to understand the OH generation mechanism.

In this paper, we have developed a multi-species, self-consistent, two-dimensional axisymmetric plasma model to analyze the effect of water content on OH production in a pulsed-dc atmospheric plasma discharge. Besides, air is taken to mean a mixture of nitrogen, oxygen, and water. Several important results are obtained and briefly summarized in this paper. Penning ionization and charge exchange ionization do not appear to play a significant role in establishing the hollow-shaped ionization of a streamer. The peak OH density increases almost linearly with water contents ranging from 0.01% to 1% and reaches 6.3×10^{18} m^{-3} when the water content is 1%. In addition, the generation and loss mechanisms of the OH radicals are also studied and discussed.

2. Model description

Our model consists of a coupled set of models: a neutral gas fluid model and a plasma dynamics model in two-dimensional axisymmetric cylindrical coordinates. In detail, steady state equations are solved for neutral gas flow, whereas

*Project supported by the National Natural Science Foundation of China (Grant No. 11465013), the Natural Science Foundation of Jiangxi Province, China (Grant No. 20151BAB212012), and the International Science and Technology Cooperation Program of China (Grant No. 2015DFA61800).

†Corresponding author. E-mail: qianmuyang@ncu.edu.cn
‡Corresponding author. E-mail: wangzhendong@ncu.edu.cn

© 2016 Chinese Physical Society and IOP Publishing Ltd

we solve time-dependent equations for plasma discharge dynamics. The schematic of the plasma jet and the simulation domain is shown in Fig. 1(a). More information about the governing equations and the boundary conditions for the neutral gas fluid and the plasma dynamic models can be found in Refs. [14] and [15] and references therein. The simulation domain extends to a radial distance of 2.3 mm from the symmetry axis. A needle tip is a semi-sphere with a radius of 0.2 mm (identified by the points AB in Fig. 1(a)). The total length of needle is 3 mm. The needle is concentric with an insulator, which has an inner radius of 1.2 mm. The dielectric constant of insulator is $5\varepsilon_0$(ε_0 is vacuum permittivity). The edges of the dielectric tube (point E) are rounded with a curvature radius of 50 μm. The needle tip is flush with the end of the tube. The gap distance between the needle tip and the dielectric surface is 3 mm. The thickness of the quartz plate (GHIJ) is 0.5 mm with relative permittivity 5 unless otherwise stated. The electrical potential is zero at the back side of the quartz plate (IJ), where a grounded metal plate is assumed to be attached. A single positive pulsed-dc voltage is applied to the needle tip (shown in Fig. 2). Besides, an external *RC* ($R = 2$ kΩ, $C = 1$ pF) circuit is assumed to be added to the plasma discharge, which is used to prevent the discharge from arcing. The working gas is pure helium flowing into the domain from the boundary between needle and the insulator tube (CD). Figure 1(b) shows the result of flow field at 1.0 standard liter per minute (SLM). As can be seen, the air mole fraction of air increases in the radial direction. Besides, the mole fractions of O_2 and N_2 have the same distribution as H_2O. As mentioned in subsequent text, the H_2O content in air is considered to be 0.01%, 0.1%, and 1%. Accordingly, the peak values of N_2 and O_2 are (0.7888, 0.2111), (0.788, 0.211), and (0.78, 0.21), respectively.

The plasma chemistry considered in this model consists of 21 different species (e, He, He^+, He_2^+, He^*, He_2^*, O_2, O_2(V), O_2(R), O_2^-, O_2^+, O_2^*, O, O^-, N_2, N_2^+, N_2(V), H_2O, H, OH, H_2O^+) and 72 elementary reactions shown in Table 1. The helium and helium–air chemistry reaction sub-mechanisms are taken from Refs. [16]–[18] and the air chemistry sub-mechanisms are taken from Refs. [8], [16], and [19]. Besides, the electron impact reaction rate coefficients for excitation and ionization as well as momentum transfer are obtained using the Boltzmann solver and fitted to analytic functions of the mean electron energy.[20] Penning ionization of O_2, N_2, and H_2O by helium metastables and charge transfer reaction are also taken into account.

All the governing equations above are solved by COMSOL with the finite element method. First, we solve fluid equations in order to obtain steady state fluid flow field of the neutral gas. Then the flow field results are coupled to the time-dependent solver, which is applied to solve the plasma dynamic equations. The complete mesh consists of 278118 cells, and the total number of degrees of freedom is about 2697479.

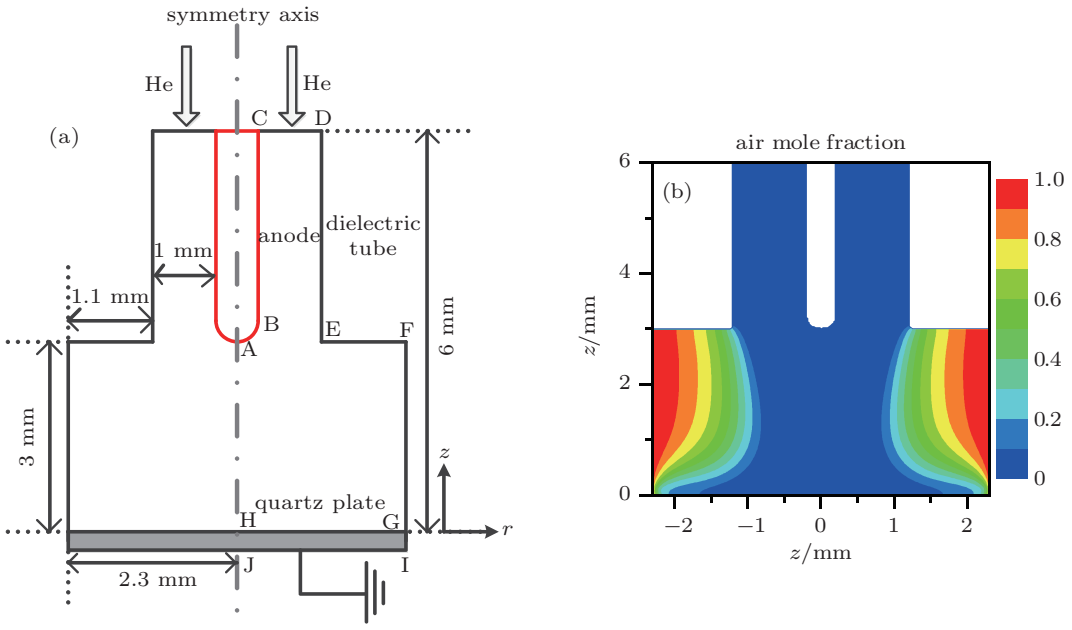


Fig. 1. (color online) (a) Side view schematics of the plasma jet and the simulation domain, (b) the air mole fraction at 1.0 SLM.

Table 1. Helium–air chemistry reactions used in this model.

helium–air chemistry (molecules-meters-electron volt)						
Rxn	Reaction	A	B	C	Activation energy	Reference
	Helium chemistry					
R1	$e + He \rightarrow e + He$		BOLSIG+		0	[20]
R2	$e + He \rightarrow e + He^*$		BOLSIG+		19.8	[20]
R3	$e + He \rightarrow 2e + He^+$		BOLSIG+		24.6	[20]
R4	$e + He^* \rightarrow 2e + He^+$	4.661×10^{-16}	0.6	4.78	4.78	[16]
R5	$e + He_2^* \rightarrow 2e + He_2^+$	1.268×10^{-18}	0.71	3.4	3.4	[16]
R6	$2He^* \rightarrow e + He^+ + He$	4.5×10^{-16}	0	0	–15.0	[16]
R7	$e + 2He^+ \rightarrow He + He^*$	5.386×10^{-13}	–0.5	0	0	[16]
R8	$He^* + 2He \rightarrow He + He_2^*$	1.3×10^{-45}	0	0	0	[16]
R9	$He^* + 2He \rightarrow He + He_2^+$	1.0×10^{-43}	0	0	0	[16]
R10	$e + He^+ \rightarrow He^*$	6.76×10^{-19}	–0.5	0	0	[16]
R11	$e + He^* \rightarrow e + He$	2.0×10^{-16}	0	0	0	[16]
R12	$2e + He^+ \rightarrow e + He^*$	6.186×10^{-39}	–4.4	0	0	[16]
R13	$e + He^+ + He \rightarrow He + He^*$	6.66×10^{-42}	-2	0	0	[16]
R14	$2e + He_2^+ \rightarrow e + He_2^*$	2.8×10^{-32}	0	0	0	[16]
R15	$e + He_2^+ + He \rightarrow 2He + He^*$	3.5×10^{-39}	0	0	0	[16]
R16	$e + He_2^+ + He \rightarrow He + He_2^*$	1.5×10^{-39}	0	0	0	[16]
R17	$2e + He_2^+ \rightarrow e + He^* + He$	2.8×10^{-32}	0	0	0	[16]
	air chemistry					
R18	$e + O_2 \rightarrow e + O_2$ (VIB3v1)		BOLSIG+		0.579	[20]
R19	$e + O_2 \rightarrow e + O_2$ (VIB4v1)		BOLSIG+		0.772	[20]
R20	$e + O_2 \rightarrow e + O_2$ (A1)		BOLSIG+		0.977	[20]
R21	$e + O_2$ (A1)$\rightarrow e + O_2$		BOLSIG+		–0.977	[20]
R22	$e + O_2 \rightarrow e + O_2$ (B1)		BOLSIG+		1.627	[20]
R23	$e + O_2$ (B1)$\rightarrow e + O_2$		BOLSIG+		–1.627	[20]
R24	$e + O_2 \rightarrow e + O_2$ (EXC)		BOLSIG+		4.5	[20]
R25	$e + O_2$ (EXC)$\rightarrow e + O_2$		BOLSIG+		–4.5	[20]
R26	$e + O_2 \rightarrow O + O^-$		BOLSIG+		3.6	[20]
R27	$e + O_2 \rightarrow e + 2O$		BOLSIG+		5.58	[20]
R28	$e + O_2 \rightarrow e + O + O$ (1D)		BOLSIG+		8.4	[20]
R29	$e + O_2 \rightarrow 2e + O + 2$		BOLSIG+		12.06	[20]
R30	$e + N_2 \rightarrow e + N_2$		BOLSIG+		0	[20]
R31	$e + N_2 \rightarrow e + N_2$ (VIBv1)		BOLSIG+		0.2889	[20]
R32	$e + N_2 \rightarrow e + N_2$ (VIB3v1)		BOLSIG+		0.8559	[20]
R33	$e + N_2 \rightarrow e + N_2$ (VIB4v1)		BOLSIG+		1.134	[20]
R34	$e + N_2 \rightarrow e + N_2$ (VIB5v1)		BOLSIG+		1.4088	[20]
R35	$e + N_2 \rightarrow e + N_2$ (A)		BOLSIG+		6.17	[20]
R36	$e + N_2 \rightarrow 2e + N_2^+$		BOLSIG+		15.6	[20]
R37	$e + H_2O \rightarrow 2e + H_2O^+$		BOLSIG+		13.5	[20]
R38	$e + H_2O \rightarrow e + H + OH$		BOLSIG+		0	[20]
R39	$O^- + O_2^+ \rightarrow O + O_2$	3.464×10^{-12}	–0.5	0	0	[16]
R40	$e + 2O_2 \rightarrow O_2 + O_2^-$	5.17×10^{-43}	–1	0	0	[16]
R41	$O_2^+ + O_2^- \rightarrow 2O_2$	2×10^{-13}	0	0	0	[16]
R42	$O_2^+ + O_2^- + M \rightarrow 2O_2 + M$	2×10^{-37}	0	0	0	[16]
R43	$O^- + O \rightarrow O_2 + e$	5×10^{-13}	0	0	0	[16]
R44	$O^- + O_2^+ \rightarrow 3O$	1×10^{-13}	0	0	0	[16]
R45	$2e + N_2^+ \rightarrow e + N_2$	3.165×10^{-30}	–0.8	0	0	[16]
R46	$e + N_2 + N_2^+ \rightarrow 2N_2$	4.184×10^{-44}	–2.5	0	0	[16]
R47	$e + H_2O^+ \rightarrow H + OH$	7.11×10^{-10}	0.5	0	0	[8]
R48	$e + H_2O^+ \rightarrow H + O + H$	3.1×10^{-10}	0.5	0	0	[8]
R49	O (1D) $+ H_2O \rightarrow OH + OH$	2.2×10^{-16}	0	0	0	[8]
R50	$OH + H + M \rightarrow H_2O + M$	4.3×10^{-37}	0	0	0	[8]
R51	$OH + OH \rightarrow H_2O + O$	2.0×10^{-18}	0	0	0	[8]
R52	$OH + O \rightarrow H + O_2$	3.32×10^{-17}	0	0	0	[8]

Table 1. (*Continued*).

Rxn	Reaction	A	B	C	Activation energy	Reference
R53	$O + H + M \rightarrow OH + M$	1.62×10^{-45}	0	0	0	[8]
R54	$O_2 + H \rightarrow OH + O$	3.55×10^{-28}	0	0	0	[8]
R55	$OH + M \rightarrow H + O + M$	4.15×10^{-88}	0	0	0	[8]
R56	$O + H_2O \rightarrow OH + OH$	2.34×10^{-31}	0	0	0	[8]
R57	$O + H \rightarrow OH$	1.0×10^{-20}	0	0	0	[19]
R58	$N_2(A) + H_2O \rightarrow OH + H + N_2$	5.0×10^{-20}	0	0	0	[19]
	helium–air interactions					
R59	$O_2^- + He_2^+ \rightarrow 2He + O_2$	1.0×10^{-13}	0	0	0	[16]
R60	$He^* + O_2 \rightarrow He + O_2^+ + e$	2.6×10^{-16}	0	0	0	[16]
R61	$He_2^* + O_2 \rightarrow 2He + O_2^+ + e$	2.6×10^{-16}	0	0	0	[16]
R62	$He^* + N_2 \rightarrow He + N_2^+ + e$	7.0×10^{-17}	0	0	0	[16]
R63	$He_2^* + N_2 \rightarrow 2He + N_2^+ + e$	7.0×10^{-17}	0	0	0	[16]
R64	$He^+ + N_2 \rightarrow He + N_2^+$	5.0×10^{-16}	0	0	0	[16]
R65	$He_2^+ + N_2 \rightarrow 2He + N_2^+$	5.0×10^{-16}	0	0	0	[16]
R66	$He^* + N_2 + He \rightarrow 2He + N_2^+ + e$	3.3×10^{-42}	0	0	0	[16]
R67	$He_2^+ + N_2 + He \rightarrow 3He + N_2^+$	1.36×10^{-41}	0	0	0	[16]
R68	$He^+ + N_2 + He \rightarrow 2He + N_2^+$	2.2×10^{-41}	0	0	0	[16]
R69	$N_2^+ + O_2 \rightarrow N_2 + O_2^+$	1.04×10^{-15}	–0.5	0	0	[17]
R70	$He^+ + H_2O \rightarrow 2He + N_2^+$	6.05×10^{-17}	0	0	0	[18]
R71	$He^* + H_2O \rightarrow He + H_2O^+ + e$	6.6×10^{-16}	0	0	0	[18]
R72	$He_2^* + H_2O \rightarrow 2He + H_2O^+ + e$	6×10^{-16}	0	0	0	[18]

Note: (i) Species 'M' in reactions R42, R50, R53, and R55 represents third-body species (He, O_2, and N_2).

(ii) The tabulated reaction rates are given in the Arrhenius form.

(iii) Units: Two-body reaction rate coefficient ($m^3 \cdot s^{-1}$), three-body reaction rate coefficient ($m^6 \cdot s^{-1}$), electron temperature T_e (eV), and gas (heavy particle) temperature T_g (K).

3. Simulation results and discussion

The typical applied waveforms of a positive half-cycle of the applied voltage and the obtained discharge current are shown in Fig. 2. Note that H_2O content in air is set to be 1% in this section. As can be seen, there are two consecutive discharge current pulses and their peak values reach 0.39 A and 0.36 A, at 27.5 ns and 29 ns, respectively. Streamer discharge characteristic parameters (electron density, electron temperature, electric field, and total ionization rate) at 27.5 ns are shown in Fig. 3, respectively. As shown in Fig. 3(a), the discharge region expands simultaneously toward radial and axial directions, and represents the hollow profile. The peak electron temperature is mainly focused at the head of the streamer, as shown in Fig. 3(b). As can be seen in Fig. 3(c), the larger space charge at the streamer front creates an enhanced electric field, causing electron avalanches, and resulting in the propagating ionization wave. Thus, the peak of electric field and electron impact ionization rate locate at the head of the streamer. The ionization rate shown in Fig. 3(d) indicates that the plasma jet propagates in the bullet mode. Since the plasma bullet runs out of the needle tip at 27.5 ns, the propagation speed of the streamer is about 7.3×10^4 m/s. Figure 4 shows the space-averaged ionization rates of electron-impact ionization of He neutral, N_2, O_2, and H_2O molecules, charge exchange and Penning ionization at 27.5 ns and 30 ns, respectively. It demonstrates that the contribution of electron-impact ionization of He and N_2 to the production of positive ions is higher than the sum of Penning and charge transfer ionization. In other words, the streamer discharge is substantially sustained by electron impact ionization, with Penning ionization and charge transfer ionization reactions being not so crucial.

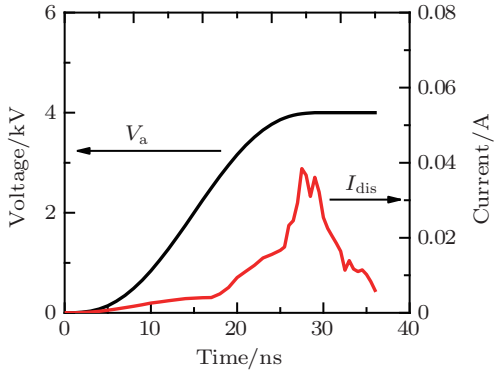


Fig. 2. (color online) Applied half-period positive pulsed-dc voltage waveform and the obtained discharge current.

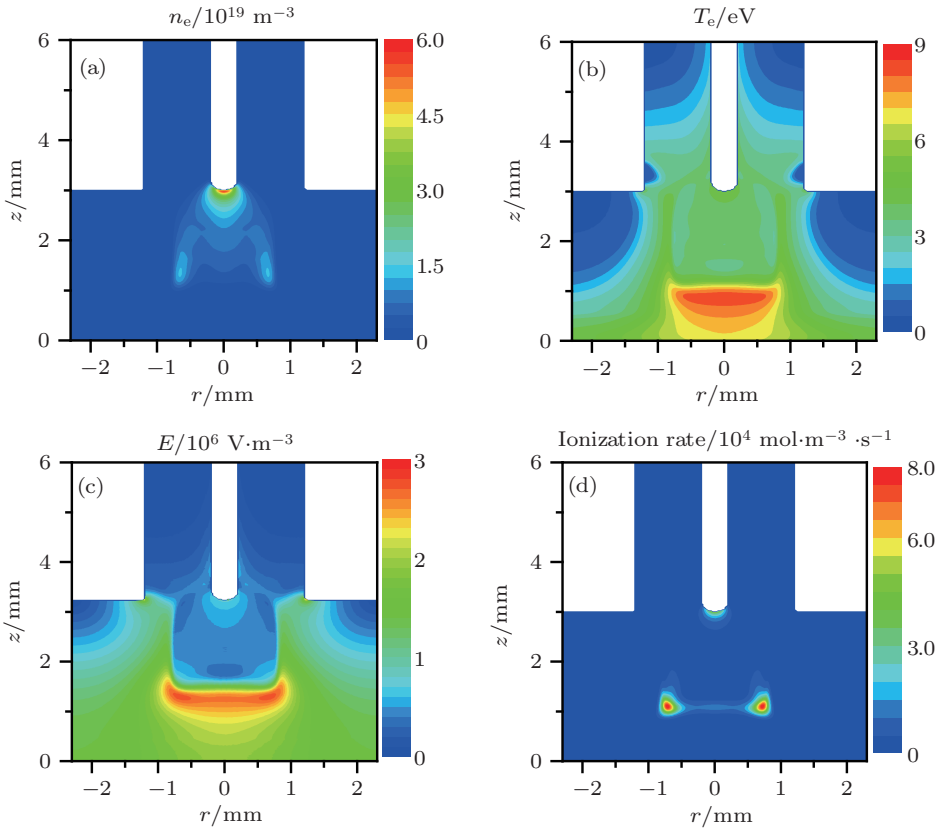


Fig. 3. (color online) Typical streamer characteristic parameters at 27.5 ns. (a) Electron density, (b) electron temperature, (c) electric field, and (d) the total ionization rate (including ionizations of He, N_2, O_2, and H_2O).

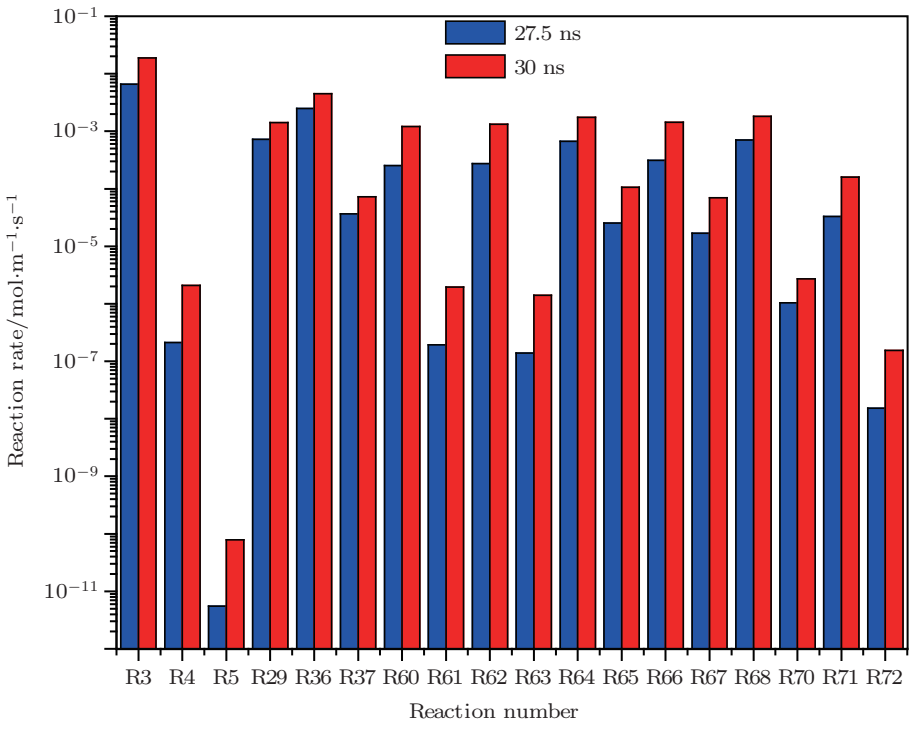


Fig. 4. (color online) Space-averaged ionization rate of helium (electron-impact ionization, R3–R5 in Table 1), O_2 (electron-impact ionization R29, Penning ionization by He^* and He_2^* (R60 and R61)), N_2 (electron-impact ionization R36, Penning ionization by He^* and He_2^* (R62 and R63), charge transfer reactions by He^+ and He_2^+ (R64, R66, R67, R68))), H_2O (electron-impact ionization R37, Penning ionization by He^* and He_2^* (R71 and R72), charge transfer reactions by He^+ (R70)).

Figures 5(a)–5(c) show the effect of H_2O contents in air 0.01%, 0.1%, and 1% on the OH density distribution, respectively. As the H_2O contents increase from 0.01% to 1%, it can be stated that the peak OH density increases linearly with the water contents and reaches 6.3×10^{18} m^{-3} when the water content is 1%, as shown in Fig. 5(d). Comparing the OH density distributions for different water contents in Fig. 5, it is found that the regions of peak OH densities remain almost the same, which can be attributed to the same H_2O density distributions in air. It is worth noting that the OH radicals also show the hollow profiles, which coincides with the experimental results reported by Lu *et al.*[8,12] In our work, we have the reason to believe that it is the hollow profile of air deduced from the neutral gas flow field (shown in Fig. 1(b)) that results in the ring-shaped OH density distribution. In order to find out the generation and loss mechanisms of the OH radicals, figure 6 shows the space-averaged reaction rates of OH production and loss reactions with the H_2O contents 0.01%, 0.1%, and 1% at 27.5 ns and 35 ns, respectively. Obviously, electron-impact dissociation of H_2O (R38, $e+H_2O \Rightarrow e+H+OH$), electron–$H_2O^+$ dissociation recombination (R47, $e+H_2O^+ \Rightarrow H+OH$), as well as dissociation of H_2O by O (1D) (R49, $O(1D)+H_2O \Rightarrow OH+OH$) are the main OH production reactions. Furthermore, during the pulse rising breakdown period ($t = 27.5$ ns), the electron-impact dissociation rate of H_2O is 1.6 and 10 times higher than electron–H_2O^+ dissociation recombination rate (R47) and dissociation of H_2O by O (1D) (R49), as shown in Fig. 6(a). Therefore, the contribution of dissociation of H_2O by electron is the dominant reaction to generate the OH radicals during the pulse rising process. However, as the voltage pulse reaches its peak and keeps constant (t=35 ns), it is shown that the contribution of dissociation of H_2O by O (1D) gradually becomes the main reaction to generate the OH radicals. The contributions of reactions R53, R54, R56, R57, and R58 to the OH radical production seem to be negligible. On the other hand, the three-body recombination reaction (R50, $H+OH+M \Rightarrow M+H_2O$) is the main loss mechanism. Besides, as the water content in air increases from 0.01% to 1%, the space-averaged reaction rate of three-body recombination increases dramatically and is comparable to those of main OH generation reactions (shown in Fig. 6). In other words, it indicates that a further increase in water content will lead to a slow increase or even a decrease in the OH density. The considerable difference between the production and loss rates of OH radicals in Fig. 6 is responsible for the long lifetime of OH radicals. The space-averaged reaction rates in Fig. 6(a) are generally one order of magnitude larger than those in Fig. 6(b), and about two orders of magnitude greater than those in Fig. 6(c), which are in good agreement with the results shown in Fig. 5(d).

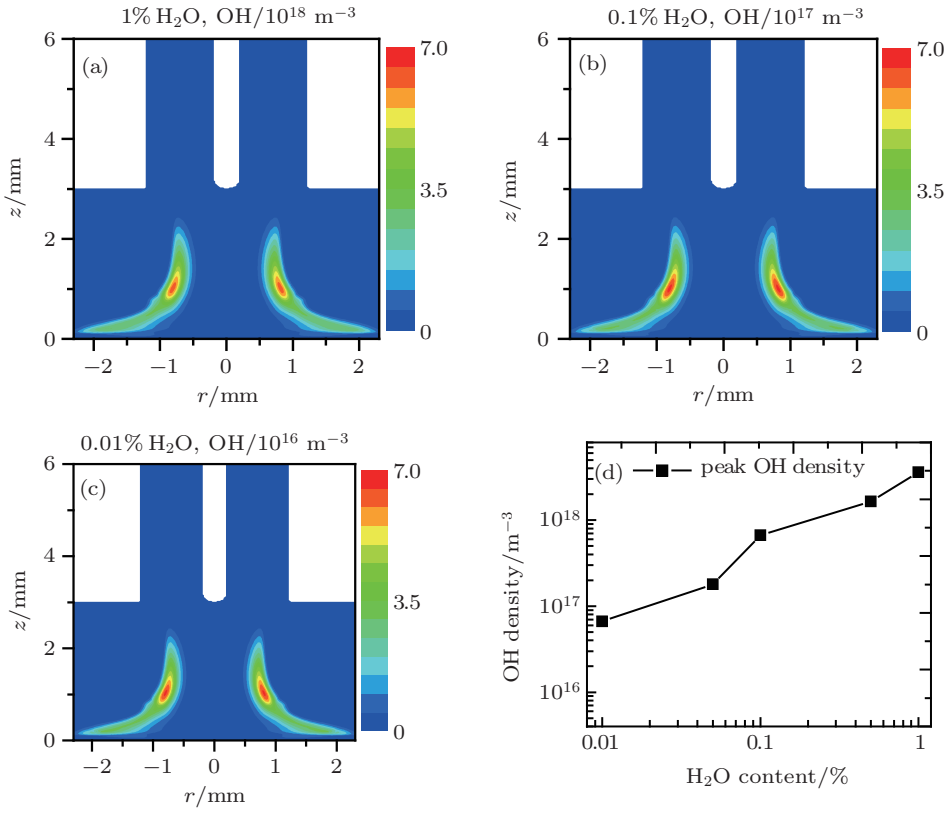


Fig. 5. (color online) OH radical density distributions at 35 ns and the H_2O contents of (a) 1%, (b) 0.1%, (c) 0.01%, (d) the variation of peak OH density with H_2O contents.

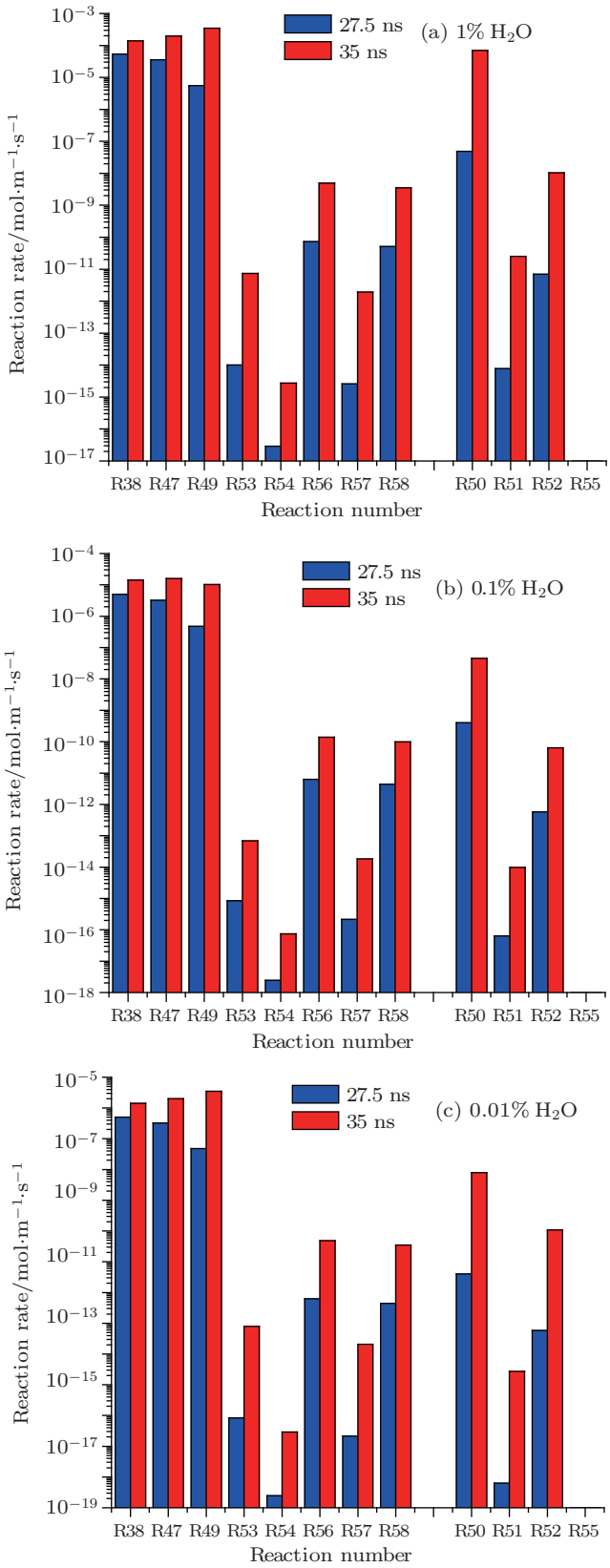


Fig. 6. (color online) Space-averaged reaction rates related to the OH production and consumption loss with the H_2O contents (a) 1%, (b) 0.1%, (c) 0.01% at 27.5 ns and 35 ns, respectively. Reactions R38–R58 are related to the OH radicals production while reactions R50–R55 are related to the OH loss.

4. Conclusions

The effect of water content on OH production in a pulsed-dc atmospheric pressure plasma jet is reported. The OH radical distribution shows the hollow profile, and the density of OH radicals increases linearly with water contents and reaches 6.3×10^{18} m^{-3} when the water content is 1%. A further increase in water content will lead to a slow increase or even a decrease in the OH density. During the pulse rising breakdown process, the electron-impact dissociation of H_2O is found to be the dominant reaction to produce OH radicals. However, as the voltage pulse reaches its peak and keeps constant, it is shown that the contribution of dissociation of H_2O by O (1D) gradually becomes the main reaction to generate the OH radicals. The present simulations suggest that the three-body recombination reaction ($H+OH+M \Rightarrow M+H_2O$) is the main loss mechanism for species OH.

References

[1] Bruggeman P and Leys C 2009 *J. Phys. D: Appl. Phys.* **42** 053001

[2] SangW L, Zhang Y T, *et al.* 2011 *Chin. Phys. B* **20** 015201

[3] Fridman G, Friedman G, Gutsol A, Shekhter A B, Vasilets V N and Fridman A 2008 *Plasma Process. Polym.* **5** 503

[4] Lu X, Naidis G V, Laroussi M and Ostrikov K 2014 *Phys. Rep.* **540** 123

[5] Huang B D, Takashima K, Zhu X M and Pu Y K 2015 *J. Phys. D: Appl. Phys.* **48** 125202

[6] Xiong Q, Lu X P, Ostrikov K, Xian Y, Zou C, Xiong Z and Pan Y 2010 *Phys. Plasmas* **17** 043506

[7] Li L, Nikiforov A, Xiong Q, Britun N, Snyders R, Lu X and Leys C 2013 *Phys. Plasmas.* **20** 093502

[8] Liu X Y, Pei X K, Ostrikov K, Lu X P and Liu D W 2014 *Phys. Plasmas.* **21** 093513

[9] Ono R and Oda T 2003 *J. Appl. Phys.* **93** 5876

[10] Ono R and Oda T 2008 *J. Phys. D: Appl. Phys.* **41** 035204

[11] Pei X K, Wu S Q, Xian Y B, Lu X P and Pan Y 2014 *IEEE Trans. Plasma Sci.* **42** 1206

[12] Pei X, Lu Y, Wu S, Xiong Q and Lu X 2013 *Plasma Sources Sci. Technol.* **22** 025023

[13] Verreycken T, van der Horst R M, Baede A H F M, van Veldhuizen E M and Bruggeman P J 2012 *J. Phys. D: Appl. Phys.* **45** 045205

[14] Qian M Y, Yang C Y, Chen X C, Ni G S, Liu S and Wang D Z 2015 *Chin. Phys. Lett.* **32** 075202

[15] Qian M Y, Yang C Y, Liu S Q, Wang Z D, Lv Y and Wang D Z 2015 *Chin. Phys. B* **24** 125202

[16] Liu X Y, Pei X K, Lu X P and Liu D W 2014 *Plasma Sources Sci. Technol.* **23** 035007

[17] Pouvesle J M, Bouchoule A and Stevefelt J 1982 *J. Chem. Phys.* **77** 817

[18] Kossyi I A, Kostinsky A Y, Matveyev A A and Silakov V P 1992 *Plasma Sources Sci. Technol.* **1** 207

[19] Bruggeman P and Schram D C 2010 *Plasma Sources Sci. Technol.* **19** 045025

[20] Hagelaar G J M and Pitchford L C 2005 *Plasma Sources Sci. Technol.* **14** 722